https://doi.org/10.1038/s44306-025-00079-y

Chaotic proliferation of relativistic domain walls for reservoir computing

J. A. Vélez[1,2] ✉, M.-K. Lee[3], G. Tatara[4], P.-I. Gavriloaea[5], J. Ross[6], D. Laroze[7], U. Atxitia[5], R. F. L. Evans[6], R. W. Chantrell[6], M. Mochizuki[3] & R. M. Otxoa[1,8] ✉

Magnetic domain walls in antiferromagnets have been proposed as key components for faster conventional information processing, thanks to their enhanced stability and ultrafast propagation. However, how non-conventional computing methods like reservoir computing might take advantage of these properties remains an open question. In this work, we show how complex domain wall patterns can form through the proliferation of multiple-domain walls from the energy stored in a single seed domain wall driven to move at a high speed close to the relativistic limit. We demonstrate that the resulting magnetic texture, consisting of up to hundreds of domain walls with an overall conserved topological charge as the initial seed domain wall, can possess chaotic spatio-temporal dynamics depending on the strength of staggered spin–orbit field induced via applied current. These findings allow us to design a multiple-domain-wall reservoir with high short-term memory and nonlinearity with respect to spin–orbit field inputs, that is suitable for ultrafast, energy-efficient, and non-conventional reservoir computing.

Antiferromagnetic materials (AFMs) have garnered significant attention due to their unique properties and potential applications in spintronic devices. Unlike ferromagnetic materials, AFMs exhibit no net magnetization, resulting in minimal parasitic fields and superior stability against external magnetic disturbances[1–5]. This inherent advantage makes AFMs highly suitable for applications where magnetic noise needs to be minimized.

Since the nineties, the study of the mobility of domain walls (DWs), vortices, and skyrmions in ferromagnets has been the flagship in spintronics because of its potential in data storage[6] and logic devices[7]. However, the principal difficulty in leveraging these technological proposals arises from the intrinsic instability of these magnetic topological defects when they exceed a certain threshold velocity. In the case of DWs in ferromagnets, this undesired dynamical regime is known as the Walker breakdown[8] and features the dynamics that combine translational and oscillatory motions[9]. Antiferromagnetic (AF) textures are not exempt from an upper limit of speed associated with the maximal group velocity of magnons, v_g[10–12]. This behavior stems from the Lorentz-invariant Lagrangian in AFMs that allows for intriguing relativistic kinematics for AF DWs, with the role of photons in conventional spacetime being replaced by magnons in magnetic systems[13,14]. However, the robustness of the DW structure is compromised when approaching the limiting speed. In particular, complex dynamical behavior, with clear Walker breakdown signatures similar to those found in ferromagnets, has also been observed in theoretical studies of layered AFMs[15–17].

Moreover, it has recently been theoretically proposed that a DW moving at relativistic speeds can produce a pair of magnons[18], in an analogous fashion with the vacuum polarization by a strong electric field in quantum electrodynamics known as the Schwinger effect[19]. In general, the energy required to observe this phenomenon is typically achievable only with large-scale experimental facilities like Hadron colliders and ultrahigh-intensity laser light sources. However, in the field of condensed matter, indirect evidence of such an effect has been reported in graphene, where the low system dimensionality allows for an increased rate of production of electron–hole pairs[20,21], in analogy with the electron–positron pair production predicted in the Schwinger effect. In an AFM, the role played by the electric field is actually taken on by the moving DW, where the energy shift due to the Doppler effect in the laboratory frame matches the energy gap for the magnon creation, leading to spontaneous emission. Regardless of the type of the driving mechanism—either spin–orbit torque (SOT)[15,22], spin-transfer torque[16], or the recently proposed laser-optical torque[23,24]— nucleation of DWs with opposite topological charges has been systematically predicted theoretically. Similar mechanisms of

[1]Donostia International Physics Center, 20018 San Sebastián, Spain. [2]Polymers and Advanced Materials Department: Physics, Chemistry, and Technology, University of the Basque Country, UPV/EHU, 20018 San Sebastián, Spain. [3]Department of Applied Physics, Waseda University, Okubo, Shinjuku-ku, Tokyo, 169-8555, Japan. [4]RIKEN Center for Emergent Matter Science (CEMS) and RIKEN Cluster for Pioneering Research (CPR), 2-1 Hirosawa, Wako, Saitama, 351-0198, Japan. [5]Instituto de Ciencia de Materiales de Madrid, CSIC, Cantoblanco, 28049 Madrid, Spain. [6]School of Physics, Engineering and Technology, University of York, York, YO10 5DD, UK. [7]Instituto de Alta Investigación, CEDENNA, Universidad de Tarapacá, Casilla 7D, Arica, Chile. [8]Hitachi Cambridge Laboratory, J. J. Thomson Avenue, Cambridge, CB3 0HE, UK. ✉e-mail: jvelez008@ikasle.ehu.eus; ro274@cam.ac.uk

topological excitation have also been observed in ferromagnetic systems, where skyrmion–antiskyrmion pairs can emerge from a single moving antiskyrmion under spin–orbit torques, leading to particle–antiparticle proliferation[25]. This magnon pair emission not only enhances our fundamental understanding of relativistic spin dynamics but also has potential practical implications for developing novel spintronics devices. However, a deeper understanding of the nucleation process remains an open question. This issue is particularly important because AF DWs moving at relativistic speed can be compressed to a few nanometers and transport energy in a fast manner[26,27], making them promising for potential device applications. Most studies to date do not explore the influence of the time-dependent driving mechanism, the problem of whether the proliferation of DWs is a chaotic process both in time and space, or ultimately the potential for generating DW patterns to perform computational tasks inspired by bio-systems.

In this work, supported by atomistic spin dynamics simulations, we theoretically show that from a seed of relativistically moving AF-DW, a pattern of multiple pairs of AF DWs can be controllably generated under the application of time-varying electric current. The spatiotemporal dynamics of DWs driven by the staggered spin–orbit field induced by AC current in layered AFMs such as Mn_2Au or CuMnAs[22,28,29], where the two magnetic sublattices are related by inversion symmetry, is analyzed in a model of one-dimensional ferromagnetic chains with mutual AF coupling. Specifically, we numerically solve the Landau–Lifshitz–Gilbert (LLG) equation, incorporating the effect of the current-induced staggered spin–orbit field as part of the effective field. Two distinct behaviors are observed depending on the strength of the spin–orbit field, with steady and periodic spin-wave emissions under weak fields and chaotic dynamics with multiple DW proliferations under strong fields. This chaotic proliferation of DWs can be understood as analogous to turbulence in fluids, where the proliferation of magnetic textures resembles the turbulent behavior propagating through space and time, driven by complex nonlinear interactions.

Based on this investigation, we propose and demonstrate the potential application of DW proliferation, interacting DWs, spin-wave emission, and the high nonlinearity of the system to the reservoir computing (RC)[30–44], which is a newly established machine-learning framework that replaces hidden layers in a recurrent neural network by a single reservoir[45–47]. The reservoir, now proposed as a texture of multiple AF DWs, plays a crucial role in nonlinearly transforming input data into an output function to solve linearly inseparable tasks[48]. We show that an array of multiple AF DWs can serve as a physical reservoir with high capacities of short-term memory (STM) and nonlinearity demonstrated in the STM and parity-check (PC) tasks, respectively, leveraging the magnetization responses excited by the input spin–orbit fields. The dependence of the performances on strength and pulse width of spin–orbit fields, as well as the position of detectors are studied systematically. These metrics provide insights into the optimization of AF-DW-based reservoirs. By combining theoretical insights from dynamical AF-DW studies with practical applications in RC, this paper aims to advance the field of spintronics and open new pathways for developing efficient, energy-conserving, and high-speed computational devices.

Results and discussion

Dynamics of domain walls

We consider two one-dimensional ferromagnetic tracks with mutual AF exchange coupling. Within each track, the initial classical magnetization configuration, $\mathbf{M}(x, t)$, at position x along the track and time t, is taken as a single steady DW, with their magnetizations being opposite in direction in the two tracks. After applying an AC current in x-direction to induce the AC staggered spin–orbit field (with amplitude proportional to current[28] and frequency assumed to be the same as the AC current) that points in opposite directions in the two tracks at each time (see the "Methods" section), the dynamics of the x-component of the DW texture in the upper track, M_x, along the track as a function of time is illustrated in Fig. 1, highlighting the

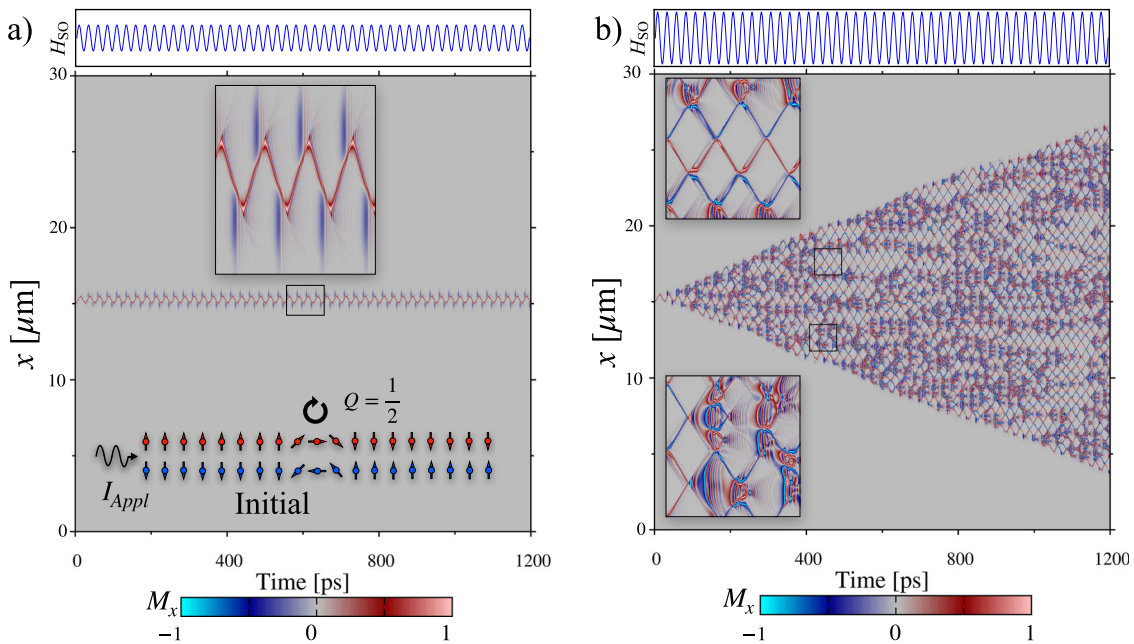

Fig. 1 | Dynamic states of domain walls. a Dynamics of M_x along the upper track as a function of time for a periodic state, with the value represented in a color gradient (gray near $M_x = 0$, pink near $M_x = 1$, and cyan near $M_x = -1$). The upper panel shows the applied spin–orbit field $H_{SO} = 74.5$ mT with a period of 25 ps. The lower inset illustrates the initial condition of the system, obtained by relaxing the domain wall, as well as the value of its topological charge ($Q = 1/2$) and the form of the AC current applied along the x-axis (I_{Appl}). The middle inset displays a magnified view of the oscillations in the DW, revealing the emission of spin waves due to the relativistic contraction of DWs. **b** Dynamics of the S_x component along the track as a function of time for a chaotic state. The upper section shows the applied spin–orbit field $H_{SO} = 78.0$ mT with a period of 25 ps. A nucleation process is observed when the DW reaches its maximal group velocity, causing the DW to contract following Lorentz transformations until a point where nucleation occurs, giving rise to new DWs while maintaining the same topological charge. The middle insets show magnified views of the DW proliferation process. The conservation of Q ensures that, despite the creation and annihilation of multiple DWs, the total topological charge of the system remains constant, which is fundamental for the integrity of the system.

differences between periodic and chaotic states in an AF system under a time-oscillating staggered spin–orbit field. In this work, the current-induced spin-transfer torque is ignored, as its effect on DW motion is prevailed by the staggered spin–orbit field, as shown recently in ref. 16. Panel 1a shows a periodic state, where the DW oscillates regularly under a spin–orbit field amplitude of H_{SO} = 74.5 mT with a period of 25 ps. The inset at the bottom of panel 1a illustrates the initial condition, depicting a 180° DW configuration and its associated topological charge Q defined by

$$Q = -\frac{1}{2\pi}\int_{-\infty}^{\infty} \nabla\phi(x,t)\,\mathrm{d}x, \tag{1}$$

where $\phi(x, t)$ represents the angle of the magnetization in the plane of each track. This topological number counts how many times the magnetization wraps around the unit circle along the DW[49], which is conserved during the time evolution of the system, ensuring that the DW structure is topologically protected and maintains its stability against external perturbations.

The upper inset in the gray area of Fig. 1a reveals a magnified view of the DW oscillations, showing the emission of spin waves. These periodic oscillations lead to spin wave emissions due to Lorentz contraction, which transports energy and angular momentum across the system. According to Shiino et al.[10], as the DW velocity approaches the maximal group velocity of spin waves, v_g, Lorentz contraction induces spin wave emission in the terahertz frequency range. The relativistic contraction of DW width Δ is described by

$$\Delta(v) = \Delta_0\sqrt{1-\left(\frac{v}{v_g}\right)^2}, \tag{2}$$

where Δ_0 = 19.8 nm corresponds to the DW width in the static state. This equation illustrates that as the DW velocity increases, its width $\Delta(v)$ decreases. This contraction is evident in the periodic oscillations as shown in the upper inset in the gray area of Fig. 1a, where the width of the red-colored region along the y-axis is larger near the motion-reversal instants at which DW velocity is smaller. The spin wave emission is also clearly observed in this simulation result. This approach highlights the connection between topology and the dynamics of DWs in AF systems, similar to what is observed in ferromagnetic systems.

Figure 1b shows a chaotic state induced by a spin–orbit field amplitude of H_{SO} = 78.0 mT with the same current oscillation period. In this regime, a complex behavior is observed where the initial DW undergoes nucleation and proliferation of new DWs. The dominant energy of the DW texture relevant to its width comes from ferromagnetic exchange ($\propto J_F$) plus easy-axis anisotropy ($\propto K_{2\perp}$) energies along the track and can be written as $E = (\gamma + 1/\gamma)E_0$ with $E_0 \propto \sqrt{J_F K_{2\perp}} \propto J_F/\Delta_0 \propto K_{2\perp}\Delta_0$ and $\gamma = 1/\sqrt{1 - v^2/v_g^2}$ is the Lorentz factor. At the initial static state, $\gamma = 1$ and the energy is $2E_0$. When the DW starts to move with Lorentz width contraction, γ increases from 1 and the energy increases from $2E_0$. Together with the energies created by the emitted spin waves, the accumulated energy increments until a critical point results in the DW breaking and subsequent nucleation of new DWs. This process reflects the dynamical instability in the system, where accumulated energy is released to create new domain structures. This instability is analogous to Walker-like breakdown in antiferromagnets, where a DW reaches a critical velocity that destabilizes its structure, leading to the formation of new magnetic textures. In our case, as the DW accelerates toward the magnonic limit, its width undergoes relativistic Lorentz contraction, concentrating energy until a threshold is exceeded, triggering the generation of soliton–antisoliton pairs and ensuring the conservation of topological charge. This mechanism has been reported in Otxoa et al.[15], where it is shown that in this highly nonlinear regime, some DWs can even reach supermagnonic velocities, exceeding the theoretical magnonic speed limit due to the breakdown of Lorentz invariance in the system's dynamics.

This phenomenon is distinct from spin wave emission since it involves the physical reconfiguration of DWs. Although spin waves do not directly cause nucleation, they influence this process by modulating local energy distribution along the track. Spin waves can interfere constructively or destructively, creating regions of high or low energy that affect DW stability and rupture points. This effect is evident in the figures, particularly in Fig. 1b, where the magnified view in the lower left corner highlights the spin wave emissions that precede the nucleation of new DWs. Frequent DW collisions occur in the chaotic state, reconfiguring DWs, altering their trajectories and velocities, and potentially leading to new DW nucleation if collision energy is sufficient to overcome local energy barriers. The figures show areas where contour lines meet and mix, indicating DW collisions and reconfigurations. The energy distribution due to spin waves is crucial in DW dynamics, as spin waves act as an additional energy dissipation channel, allowing DWs to release accumulated energy. However, when this dissipation is insufficient, the remaining energy can lead to DW rupture and nucleation. The balance between spin wave emission and DW nucleation defines the complexity of the chaotic state observed.

In summary, Fig. 1 provides a comprehensive view of the transition between periodic and chaotic DW behavior in an antiferromagnetic system under an applied spin–orbit field. The distinction between spin wave emission and nucleation processes is clearly highlighted, offering a deep understanding of the dynamic mechanisms involved. Periodic oscillations result in spin wave emission that dissipates energy, whereas in the chaotic state, energy accumulation leads to DW rupture and nucleation. DW collisions and the influence of spin waves on energy distribution add another layer of complexity to the system's dynamics.

In order to capture the details of spatio-temporal dynamics of the system of DWs combined with spin waves, we use fast Fourier transform (FFT) to analyze the magnetizations as follows. Figure 2a, b are enlarged views of M_x corresponding to the periodic state in Fig. 1a and the chaotic state in Fig. 1b, respectively. In Fig. 2a, stable dynamics are observed as the spin wave emission occurs in a repetitive manner in time with a fixed period. The FFT of time evolution of M_x at each position into frequency-space is shown in Fig. 2b, displaying distinct peaks characteristic of periodic motion. Specific oscillation nodes are observed, indicating both spatial and temporal regularity in the system. To confirm this expectation, the time evolution of M_x averaged along the entire track is shown in Fig. 2c, and regular oscillations synchronized with the applied field are observed. The FFT of the spatially averaged M_x presented in Fig. 2d corroborates the periodic magnetization oscillations in time with a pattern of regular peaks in the frequency domain highlighting the deterministic behavior of the DW dynamics.

On the other hand, Fig. 2e depicts the dynamics of M_x in a chaotic state. The dynamics reveal the proliferation and annihilation of DWs and their complex interactions, indicating chaotic behavior in both space and time. The FFT of M_x is presented in Fig. 2f, revealing peaks smeared in a broad and continuous distribution of frequencies, which is typical of a chaotic state that reflects the irregular and non-repetitive nature of magnetization dynamics. This complexity in the frequency domain indicates the absence of a dominant pattern and shows a superposition of multiple oscillation modes that are interacting nonlinearly. This chaotic dynamics is highly sensitive to initial conditions and external perturbations. The presence of multiple peaks in the FFT spectrum suggests the existence of various temporal and spatial scales in the DW dynamics. The spatial average of M_x being irregular in time as shown in Fig. 2g again confirms this behavior. The FFT of this average value, presented in Fig. 2h, reveals a broad and complex frequency spectrum, indicating the nonlinear and chaotic dynamics of the system.

Figure 3 illustrates the phase transitions of the dynamics of our AF DWs represented by a bifurcation diagram. To survey the dependence of magnetization dynamics on the excitation spin–orbit field, we calculate two primary dynamic indicators as the growth rate of new DWs, ξ, and the

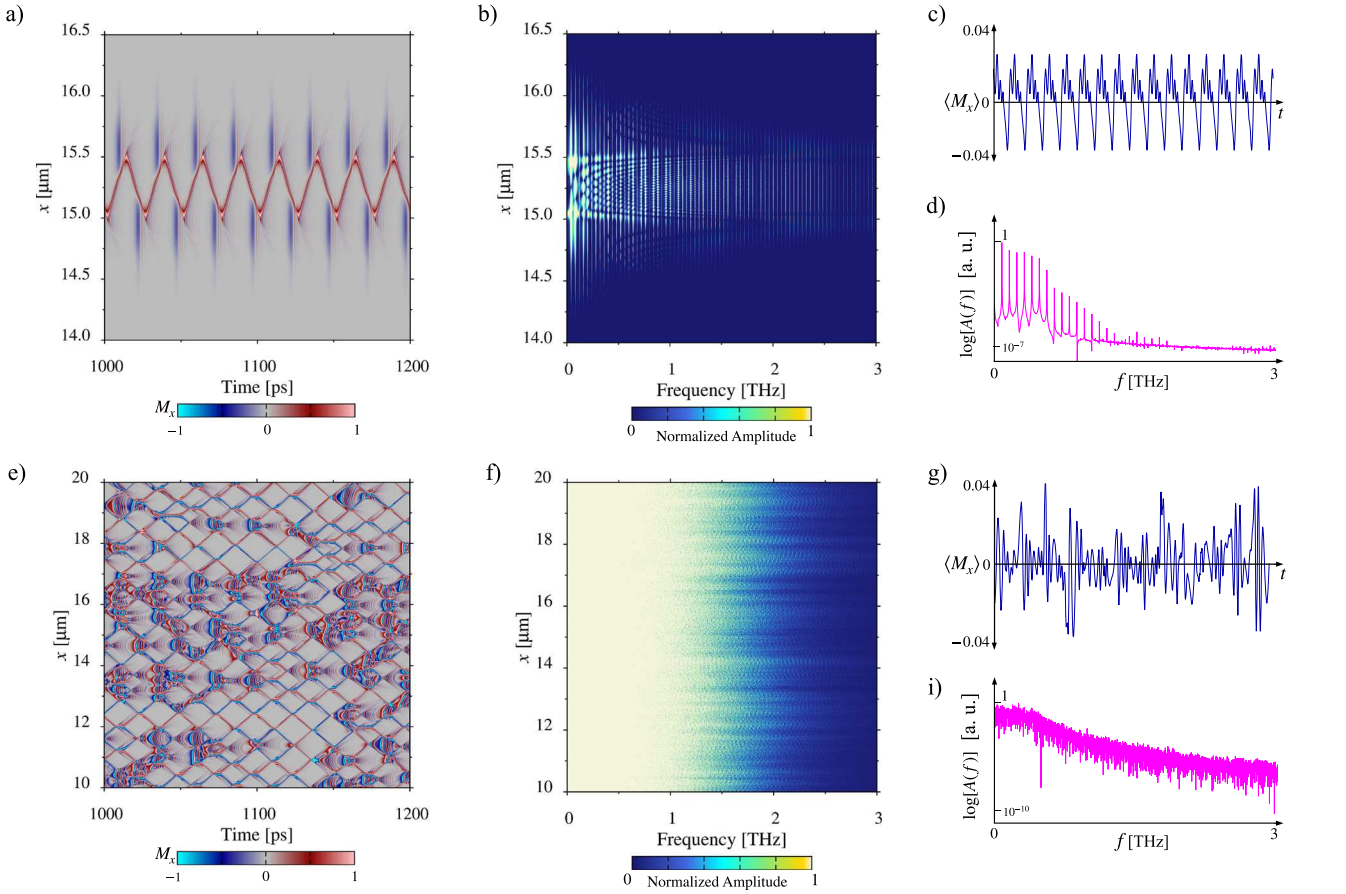

Fig. 2 | Soliton proliferation. a Dynamics of M_x along the upper track as a function of time for a periodic state as an enlarged view of Fig. 1a. **b** Fast Fourier transform (FFT) of the temporal evolution of $M_x(x, t)$ at each spatial position from panel (**a**), transforming the time-space data into frequency-space. Periodic nodes are observed in both time and position. **c** Mean value of M_x along the upper track as a function of time, showing the stability of the dynamics in the periodic state. **d** FFT of the mean value of M_x, indicating global periodic behavior. **e** Enlarged view of M_x for the chaotic state in Fig. 1b. **f** FFT of M_x in panel (**e**), showing a broad spectrum of frequencies characteristic of chaotic dynamics. **g** Mean value of M_x as a function of time for the chaotic state, highlighting the complexity of the dynamics. **h** FFT of the mean value of M_x, revealing the broad frequency spectrum typical of chaotic states.

complexity, C, which allow us to characterize the transition between periodic and chaotic states as a function of various field amplitudes H_{SO} from 65 to 85 mT in an interval of 0.5 mT, and periods $T = 15, 20, 25, 30$ ps. In Fig. 3a, we illustrate the chaotic dynamics of the DWs and their proliferation process. An analogy can be drawn to the turbulence model in fluid mechanics, where magnetic textures proliferate in space and time in a manner similar to vortexes in a turbulent fluid. This detailed view enables us to clearly observe the complex interactions and reconfiguration of the DWs. In Fig. 3b, we present the number of detected DWs as a function of time, represented by blue points. The pink points indicate the moving average of the number of DWs, calculated by averaging over a window of 100 time steps starting just when the DWs begin to nucleate that is, after a transient period during which the DW still oscillates without nucleation. This approach allows us to smooth out rapid fluctuations and highlight general trends in the proliferation of DWs. The green line shows a linear fit of these averaged points. The observed fluctuations highlight the nucleation and annihilation processes of DWs, emphasizing the nonlinear dynamics of the system.

Figure 3c shows the topological configuration of DWs at three instants labeled by I–III in Fig. 3a. Above each DW texture, their topological charge Q is indicated, revealing that DWs are produced in pairs with opposite topological numbers, such that the net Q is conserved in time as shown in the right panel of Fig. 3c. Hence, despite the chaotic proliferation and complex dynamics, the system remains in the same topological class at all times.

Figure 3d presents a characterization of the dynamical behaviors of the system based on two complementary indicators: a bifurcation diagram (lower panel) and a phase diagram (upper panel). These indicators provide insight into the transitions between periodic and chaotic regimes in the DW dynamics as a function of the spin–orbit field amplitude H_{SO} and the oscillation period T. The lower panel of Fig. 3d displays the bifurcation diagram, where the DW nucleation rate ξ is extracted from the slope of the linear fit of the moving average in Fig. 3b. This slope quantifies the growth rate of the number of DWs per unit time. The spin–orbit field strength is varied from $H_{SO} = 65$ mT to $H_{SO} = 85$ mT in steps of $\Delta H_{SO} = 0.5$ mT for four different excitation periods T. The linear fits reveal that the nucleation rate follows a proportional trend with the field amplitude, expressed as $\xi = a_i H_{SO} + b_i$. The values of a_i, which represent the sensitivity of the nucleation rate to variations in H_{SO}, are given by $a_i = \{10.538, 7.86, 6.78, 5.56\}$ mT^{-1} for $T = \{15, 20, 25, 30\}$ ps, respectively. The bifurcation diagram allows us to track the transition from a periodic to a chaotic regime, where $\xi = 0$ corresponds to a periodic state with no nucleation, and $\xi > 0$ indicates the onset of chaotic proliferation of DWs.

The upper panel of Fig. 3d presents a phase diagram where the complexity indicator C is used to distinguish between periodic and chaotic dynamics. The classification is performed using two distinct markers: purple squares represent $C = 0$, indicating periodic dynamics, while green circles correspond to positive complexity values, signaling chaotic behavior. The complexity measure, which combines entropy and disequilibrium, quantifies the degree of order in the system (see Supplementary Material for details)[50]. The diagram reveals that the system exhibits a transition between

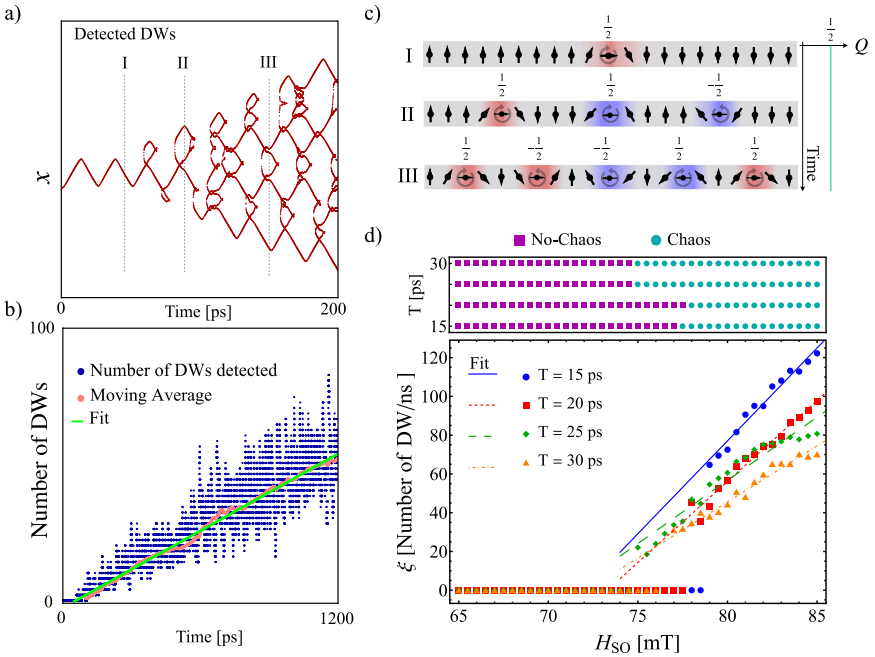

Fig. 3 | Phase diagram. a Illustration of the chaotic dynamics of the DW and its proliferation process, using an analogy with the vortex model in fluid mechanics. This model facilitates the visualization and understanding of the complexity of DW behavior in the AF system. Labels I–III indicate specific moments at which the topological configuration is schematically shown in panel (**c**). **b** Number of DWs detected as a function of time. The blue points represent the number of DWs detected at each time instant. The pink points show the moving average of the number of DWs, which smooths out fluctuations and allows for a better interpretation of the overall trend. The green line is a linear fit of the moving average points, indicating the growing trend of the number of DWs over time. **c** Topological configuration of the DWs at instances I–III marked in panel (**a**). Each row shows the DWs at different time instants, highlighting the conservation of the topological charge Q. The numerically extracted time dependence of the topological charge is illustrated on the right side of the panel, showing that Q is conserved over time despite the proliferation of new DWs. The color code represents the magnitude of M_x with blue for $M_x = -1$, red for $M_x = 1/2$, and gray for $M_x = 0$. **d** Bifurcation diagram representing the DW nucleation rate ξ as a function of the spin–orbit field strength H_{SO} and oscillation period T. The nucleation rate ξ is extracted from the slope of the linear fit of the moving average in panel (**b**), which quantifies the growth rate of the number of DWs per unit time. The spin–orbit field strength is varied from $H_{SO} = 65$ mT to $H_{SO} = 85$ mT in steps of $\Delta H_{SO} = 0.5$ mT for four different excitation periods T, allowing us to track the transition in nucleation dynamics. The upper section of panel (**d**) presents a phase diagram characterizing the transition between periodic and chaotic behaviors based on the complexity indicator C. Purple squares correspond to $C = 0$, indicating periodic dynamics, whereas green circles represent positive complexity values, signaling chaotic behavior. This classification reveals how the system transitions between periodic and chaotic regimes as H_{SO} and T are varied.

periodic and chaotic regimes as a function of both H_{SO} and T, with lower T values favoring a chaotic response. Interestingly, despite the strong correlation between the complexity C and the nucleation rate ξ, certain regions in the diagram show cases where $\xi = 0$ while $C > 0$, indicating that the system remains chaotic even when no new DWs are nucleated. This suggests that the magnetization dynamics can retain chaotic features without additional DW proliferation, highlighting the intricate interplay between topological excitations and dynamical complexity in the system.

Altogether, Figs. 1–3 offer a comprehensive view of how the AC staggered spin–orbit field influences both the nucleation rate and complexity of the system to induce the phase transition of the DW configuration and dynamics between periodic and chaotic phases. The nucleation process we observe is neither linear in time nor predictable, as it depends on local fluctuations of energy. The instability suffered by the relativistically moving DW disturbs its regular motion and texture, and eventually producing spin waves and new DWs to release energy, which interact with each other nonlinearly. This creates an environment where small variations can generate significant changes in the system dynamics and result in chaotic behavior. In summary, the interplay of relativistic contraction, energy accumulation, and nonlinear interactions between DWs and spin waves induces chaotic dynamics during the nucleation process. This is reflected in the positive complexity observed in chaotic states, even in the absence of new DW proliferations. In these cases, chaos manifests through irregular and sensitive movements of the existing DWs, induced by nonlinear interactions and energetic fluctuations, without necessarily involving additional nucleations.

These observations not only deepen our understanding of chaotic DW dynamics but also provide insight into their potential functional implications. These results reinforce our understanding of how relativistic contraction, spin wave emissions, and nonlinear interactions collectively regulate the stability of domain walls in antiferromagnetic systems. The transition between periodic and chaotic regimes, quantified through complexity measures and DW proliferation rates, highlights the fundamental role of energy accumulation and dissipation in the evolution of these magnetic textures. Beyond its theoretical significance, the ability to induce and control chaotic dynamics in these systems suggests that these phenomena could be leveraged in advanced spintronic applications, such as the development of magnonic architectures requiring highly nonlinear and adaptive responses.

Reservoir computing

After investigating the chaotic DW proliferation driven by staggered spin–orbit field in AFMs, in this section, we propose the potential of a proliferated multiple-DW configuration as a viable system for spintronics reservoir computing (RC) by demonstrating the possession of short-term memory and nonlinearity inherent in the magnetization responses to external spin–orbit field inputs in this system. We consider two one-dimensional ferromagnetic layers with mutual AF exchange coupling, as illustrated in Fig. 4a. Each layer has a length of 6000 sites and contains seven equally spaced DWs with centers located at site indices $750n$ with $n = 1, 2, \ldots, 7$ (see Fig. 4b). Each neighboring DWs have opposite winding numbers, mimicking the texture generated by the chaotic proliferation from a single

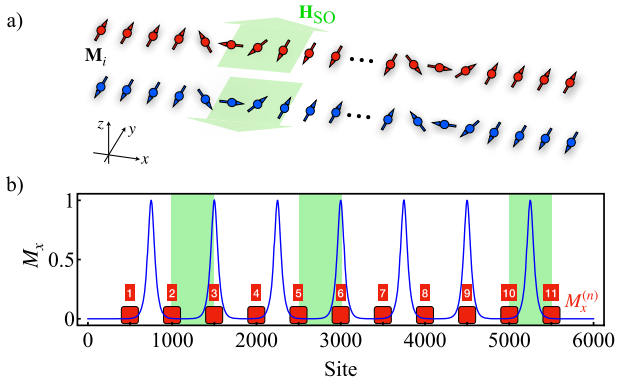

Fig. 4 | Schematics RC. a Schematics of the bilayer AF-DW system for RC. Black arrows indicate the local magnetization vectors and the green thick arrows are the local input SO-fields. **b** Initial configuration of the *x*-component of the DW magnetizations in the upper layer (blue curve). For the lower layer, the sign of M_x is the opposite. Green shaded zones are input areas and the eleven detectors are labeled by red boxes.

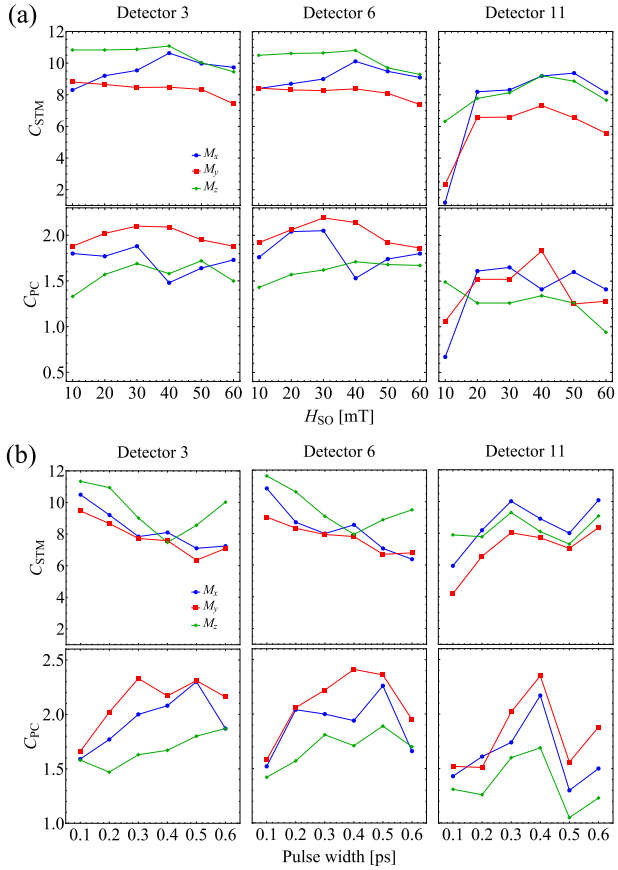

Fig. 5 | RC results. Comparison of the capacities as functions of **a** SO-field amplitude and **b** SO-field pulse width for the three best detectors: 3, 6, and 11.

seed DW that preserves the topological number. We evaluate the performance of this system on two benchmark tasks of RC as the short-term memory (STM) and parity-check (PC) tasks[31,34,41].

For both tasks, the input data $s_{in}(T_i)$ consists of a sequence of random digits, either 1 or 0, at integer time steps T_i. The goal of RC by using this DW system is to predict specific transformations of the inputs by an output function, taken as a linear combination of the magnetization responses measured on local areas in the DW-array. The correspondence between input digits and physical excitations in the DW system is designed as follows. When $s_{in}(T_i) = 1$, we simultaneously apply three local staggered spin–orbit field pulses in $\pm y$-direction for the upper and lower DW array, respectively. These pulses are applied to three input areas located on site indices from 1001 to 1500, 2500 to 3000, and 5001 to 5500, as indicated by green areas in Fig. 4b. When $s_{in}(T_i) = 0$, we reverse the directions of the spin–orbit field pulses for both layers and apply them on the same local areas with the same pulse width. The surveyed pulse width of spin–orbit field ranges from 0.1 to 0.5 ps, while its magnitude is varied from 10 to 60 mT in this study.

We placed 11 detectors on the DW array as shown in Fig. 4b. In the area of each detector, the averaged magnetization at a number of virtual-node temporal instants in each spin–orbit field pulse is recorded to define the reservoir state vector. A linear transformation of the measured magnetizations is defined as an output function, with the coefficients being the weight vector components being optimized to minimize the mean square error between the target and output for a training set of random digits. The optimized weight vector is then taken to predict another testing set of digits by their magnetization responses (see details in the "Methods" section). The target functions for STM and PC tasks are respectively defined in Eqs. (6) and (7) in the "Methods" section. From these definitions, the STM task investigates to what extent the input at a previous time $T_i - T_{delay}$ can be reconstructed by the reservoir state at current time T_i, which is important for applications such as sentence prediction and speech recognition[45–47] that involve time-series data. Meanwhile, the PC task examines to what extent the reservoir can nonlinearly transform its components into a summation of past inputs modulo 2, which is essential for problems like pattern classification and hand-written digit recognition[42–44] that require nonlinearity.

After the training procedure, the squared correlation between the testset targets and outputs for each detector is calculated. As shown in Supplementary Fig. 4, empirically we find when a detector is placed close to both the edge of any input areas, and either to one of the DW centers (e.g., detectors 3 and 6 in Fig. 4b) or near the system edge (e.g., detectors 11), a better-squared correlation is obtained for both tasks. This indicates the need for both a large spatial gradient of H_{SO} and either a large gradient of M_y or strong spin wave reflection near the system edge, to excite significant magnetization responses that possess memory and nonlinearity relative to the input. To quantify the performance, we calculate the capacities $C_{STM(PC)}$ for STM (PC) tasks[31,34,41] for better detectors 3, 6, and 11, defined as the sum of the squared correlations from $T_{delay} = 1$ to 30. A larger capacity indicates a better performance by the reservoir. We note that in literature many works calculate the capacity including the point of $T_{delay} = 0$. Since the squared correlation at $T_{delay} = 0$ is trivially close to 1, we exclude this point to estimate the capacity in a stricter way, following ref. 34. We achieve the highest C_{STM} and C_{PC} values of approximately 10.5 and 1.5, respectively, comparable with other spintronics reservoirs using a similar number of virtual nodes [31,34,36,41]. This finding clearly demonstrates the potential of a multiple-DW array proliferated by spin–orbit field in AFMs for applications in physical reservoir computing. We have tested the reproducibility by performing sequential runs of the tasks and compared the performances between the proposed multiple-DW array and a pure AF state without DW textures and find the multiple-DW array shows much better results (see the "Methods" section for details).

To investigate the potential input dependence of the performance, we compare the capacities carried out by different components of magnetizations under varying pulse widths and amplitudes of spin–orbit field, as illustrated in Fig. 5. In Fig. 5a, the pulse width is fixed at 0.2 ps for all curves. The results show that increasing the field amplitude from 10 to 60 mT does not significantly change the capacities. For $H_{SO} = 10$ mT, the capacities carried out by M_x and M_y components were lower than those for higher SO-field amplitudes. Interestingly, the data reveals a contrasting behavior between the STM and PC capacities. Specifically, the M_z component has roughly better results for STM capacities compared to M_x and M_y. On the contrary, for PC capacities, M_z is worse than the other components. This opposite behavior between STM and PC capacities is reminiscent of the

empirical law of memory-nonlinearity trade-off[51,52], which is frequently observed in dynamical models or physical systems in RC, suggesting that the introduction of nonlinearity into reservoir dynamics tends to degrade memory capacity.

In Fig. 5b, we study how the capacities for STM and PC tasks change with different pulse widths, ranging from 0.1 to 0.6 ps. For detectors 3 and 6, as the pulse width increases from 0.1 and 0.4 ps, the STM capacities tend to decrease, while the PC capacities increase. This opposite behavior is another indication of a memory-nonlinearity trade-off, where an increase in one capacity typically leads to a decrease in the other. However, detector 11 exhibits a unique behavior. As the pulse width increases, both STM and PC capacities follow a similar trend, which violates the expected trade-off. This suggests that for detector 11, it may be possible to simultaneously enhance the short-term memory and nonlinearity by fine-tuning the input pulse width. This capability is particularly advantageous for machine-learning tasks since many realistic problems require both memory and nonlinearity. The common trade-off between memory and nonlinearity limits the learning potential of reservoirs, making our finding significant. This distinct behavior of detector 11 as compared to detectors 3 and 6 may be attributed to the edge effects of the system. These edge effects might enhance both memory and nonlinearity due to phenomena like spin wave reflection and interference occurring near the system edge. It is left for our future work to find concrete ways to overcome the memory-nonlinearity trade-off and to enhance capacities for both STM and PC tasks in this multiple-DW reservoir.

The results presented in this work demonstrate the strong potential of DW-based reservoirs in antiferromagnetic systems, where the interplay between chaotic DW dynamics and spin wave interactions enables efficient and tunable computational performance. The ability to reconfigure the reservoir by adjusting the amplitude and period of the spin–orbit field provides a mechanism to optimize memory and nonlinearity trade-offs, a fundamental challenge in RC. Furthermore, our findings highlight how the mechanisms governing chaotic DW proliferation, previously analyzed in detail, play a crucial role in enhancing the diversity and richness of dynamical responses in the reservoir. This connection between DW chaos and computational capacity suggests that DW proliferation dynamics could be leveraged to improve the performance of physical reservoirs in spintronic systems. While these results represent an initial step, future research could explore strategies to optimize the interaction between DW dynamics and input parameters, with the goal of enhancing the efficiency and stability of these systems in neuromorphic computing applications.

Methods

Theoretical model

The system under study is the layered collinear antiferromagnet, Mn_2Au, characterized by its good conductivity, strong magnetocrystalline anisotropy, and a Néel temperature well above room temperature. These intrinsic properties make this material ideal for exploring the dynamics of antiferromagnetic domain walls due to its intrinsic properties.

The total energy of the system includes contributions from exchange interactions, magnetocrystalline anisotropy, and the spin–orbit field induced by an alternating current. The configurational energy E can be expressed as

$$\begin{aligned} E &= -\sum_{\langle i,j\rangle}\mathcal{J}_{ij}\mathbf{M}_i\cdot\mathbf{M}_j - K_{2\perp}\sum_i(\mathbf{M}_i\cdot\hat{z})^2 \\ &\quad -K_{2\parallel}\sum_i(\mathbf{M}_i\cdot\hat{y})^2 - \tfrac{K_{4\perp}}{2}\sum_i(\mathbf{M}_i\cdot\hat{z})^4 \\ &\quad -\tfrac{K_{4\parallel}}{2}\sum_i\left[(\mathbf{M}_i\cdot\mathbf{u}_1)^4+(\mathbf{M}_i\cdot\mathbf{u}_2)^4\right] \\ &\quad -\mu_0\mu_s\sum_i\mathbf{M}_i\cdot\mathbf{H}^i_{\mathrm{SO}} \end{aligned} \tag{3}$$

where $\mathbf{S}_i$ is the spin vector at site i, $\mathcal{J}_{ij}$ represents the exchange interaction between spins i and j with $\mathcal{J}_1 = -5.468\times10^{-21}$ J, $\mathcal{J}_2 = -7.347\times10^{-21}$ J, $\mathcal{J}_3 = 1.587\times10^{-21}$ J, $K_{2\perp}$ and $K_{2\parallel}$ are the second-order magnetocrystalline anisotropy constants in the perpendicular and parallel directions, respectively, with $K_{2\perp} = -1.303\times10^{-22}$ J, $K_{2\parallel} = 7K_{4\parallel}$, $K_{4\perp}$, and $K_{4\parallel}$ are the fourth-order magnetocrystalline anisotropy constants in the perpendicular and parallel directions, respectively, with $K_{4\perp} = 2\,K_{2\parallel}$, $K_{4\parallel} = 1.855\times10^{-25}$ J, and $\mathbf{H}^i_{\mathrm{SO}}$ is the spin–orbit field at site i, induced by the alternating current. The unit vectors $\hat{u}_1$ and $\hat{u}_2$ represent the in-plane xy-based directions, with $\mathbf{u}_1 = [110]$ and $\mathbf{u}_2 = [1\bar{1}0]$.

The spin–orbit field ($\mathbf{H}^i_{\mathrm{SO}}$) is induced by an alternating current flowing in the x-direction. Due to the spin–orbit interaction, this current generates a spin–orbit field in the y-direction. This field can be described as $\mathbf{H}^i_{\mathrm{SO}} = H_{\mathrm{SO}}\sin(\omega t)\hat{y}$, where H_{SO} is the amplitude of the field, ω is the angular frequency, and t is the time. This field introduces an additional interaction that affects the spin dynamics in the material. To describe the temporal evolution of the spins under the influence of the aforementioned fields, we use the Landau–Lifshitz–Gilbert (LLG) equation:

$$\frac{d\mathbf{M}_i}{dt} = -\gamma\mathbf{M}_i\times\mathbf{H}^{\mathrm{eff}}_i - \gamma\alpha\mathbf{M}_i\times(\mathbf{M}_i\times\mathbf{H}^{\mathrm{eff}}_i) \tag{4}$$

where γ is the gyromagnetic ratio of the free electron (2.21×10^5 m/A s), $\alpha = 0.001$ is the Gilbert damping parameter, and $\mathbf{H}^{\mathrm{eff}}_i$ is the effective field resulting from all the interaction energies.

The effective field $\mathbf{H}^{\mathrm{eff}}_i$ is obtained by differentiating the total energy E with respect to $_i$: Corrected $\mathbf{S}_i$ to $\mathbf{M}_i$ to maintain consistency with the notation used in the effective field expression.

$$\mathbf{H}^{\mathrm{eff}}_i = -\frac{1}{\mu_0\mu_s}\frac{\delta E}{\delta\mathbf{M}_i}. \tag{5}$$

This includes contributions from exchange interactions, anisotropy, and the spin–orbit field.

This theoretical model provides a solid foundation to explore the dynamics of domain walls in the antiferromagnetic system Mn_2Au under the influence of an alternating current. By considering all energy contributions and using the Landau–Lifshitz–Gilbert equation, we can simulate and analyze how these factors influence the temporal evolution of the domain walls. This analysis offers valuable insights for the development of reservoir computing applications and other advanced spintronic technologies.

Reservoir computing method

The commonly adopted target functions y_{target} for the STM and PC tasks are defined as[31,34,41]

$$\begin{aligned} y^{\mathrm{STM}}_{\mathrm{target}}(T_i, T_{\mathrm{delay}}) &= s_{\mathrm{in}}(T_i - T_{\mathrm{delay}}), \\ y^{\mathrm{PC}}_{\mathrm{target}}(T_i, T_{\mathrm{delay}}) &= \left[s_{\mathrm{in}}(T_i) + s_{\mathrm{in}}(T_i-1)\right. \end{aligned} \tag{6}$$

$$\left. +\cdots + s_{\mathrm{in}}(T_i - T_{\mathrm{delay}})\right] \bmod 2, \tag{7}$$

where T_{delay} is a dimensionless integer delay time, and $s_{\mathrm{in}}(T_i - T_{\mathrm{delay}})$ is the input digit (0 or 1) at a previous integer time of $T_i - T_{\mathrm{delay}}$. We placed 11 detectors located at sites $501 + 500n$ with $n = 0, 1, \ldots, 10$ on the DW array as shown in Fig. 4b. All detectors have a short length of 11 sites that corresponds to roughly 3.7 nm taking the lattice constant of Mn_2Au, which is nearly $\Delta_0/5$, in order to capture the possible variation of the performance carried out by magnetizations located at different positions inside or outside the DW region. For each detector, we measured their averaged magnetization at a number of N_{vn} virtual-node temporal instants in the interval from T_ip to $(T_i+1)p$ with p being the spin–orbit field pulse width, to define a reservoir state vector at time T_ip as $\mathbf{R}^{(n)}_j(T_i) \equiv \Big(\langle M^{(n)}_j(T_ip + p/N_{\mathrm{vn}})\rangle, \langle M^{(n)}_j(T_ip + 2p/N_{\mathrm{vn}})\rangle., \ldots, \langle M^{(n)}_j((T_i+1)p)\rangle\Big)$, with $j = x, y, z$ labeling the component of 11 magnetizations $\mathbf{M}^{(n)}$ inside the nth detector area, and $\langle\ldots\rangle$ denoting the average over the eleven sites within this detector. The scalar output function $y^{(n)}_{j,out}$ is defined as a dot product between this N_{vn}-

dimensional reservoir vector and a weight vector with the same dimension, $\mathbf{W}_j^{(n)}$, then plus a constant bias $W_{j,0}^{(n)}$, namely $y_{j,out}^{(n)} = \mathbf{W}_j^{(n)} \cdot \mathbf{R}_j^{(n)} + W_{j,0}^{(n)}$. The number of components in the weight vector that are required for training is thus $N_{\rm vn} + 1$, including one for the constant bias. Note that the weight vectors $\mathbf{W}_j^{(n)}(T_{\rm delay})$ differ among the delay times $T_{\rm delay}$, the 11 detector positions, and the magnetization components $j = x, y, z$. They are required to be trained independently for each delay time, each detector, and each component.

In simulation, the DW system is initially relaxed for a sufficiently long time until magnetizations are almost fixed in time. Then for each delay time $T_{\rm delay} = 0, 1, \ldots$ separately, we stabilize the response of this system by first injecting 1000 random inputs of 1 or 0 via the corresponding sequence of SO-field pulses, then we take the following 100 random inputs for training, and their subsequent 50 inputs for testing. The training is done by minimizing the mean square error between the targets in Eqs. (6) and (7)) and the output function $y_{j,out}^{(n)}$ using the pseudo-inversed matrix method[53,54] for the 100 training dataset, after which, the optimal weight vector is used to form the output function of another distinct 50 testing inputs. The squared correlation between target and output[31,34,41] is then calculated as

$$\mathrm{Corr}_{\rm STM(PC)}^{(n,j)}(T_{\rm delay}) = \frac{\mathrm{Cov}^2[y_{\rm target}^{\rm STM(PC)}(T_i, T_{\rm delay}), y_{j,\rm out}^{(n)}(T_i)]}{\mathrm{Var}[y_{\rm target}^{\rm STM(PC)}(T_i, T_{\rm delay})]\mathrm{Var}[y_{j,\rm out}^{(n)}(T_i)]}, \quad (8)$$

with

$$\begin{aligned} \mathrm{Cov}[A(T_i), B(T_i)] &= \tfrac{1}{N}\textstyle\sum_i (A(T_i) - \bar{A})(B(T_i) - \bar{B}), \\ \mathrm{Var}[A(T_i)] &= \tfrac{1}{N}\textstyle\sum_i (A(T_i) - \bar{A})^2, \end{aligned} \quad (9)$$

for generic functions, A and B, where Cov and Var denote the covariance and variance, respectively, $\bar{A}$ is the average of $A(T_i)$ over all T_i, and N is the number of time steps T_i. The standard squared correlation Corr takes a value within a range of [0,1], and a larger value indicates better fitting of the targets by outputs.

To quantify the performance of our DW-array reservoir, we calculate the capacity, which is defined as the summation of squared correlations from $T_{\rm delay} = 1$ to 30, excluding contributions from the delayed memory with peaks located at finite $T_{\rm delay}$ (see Supplementary Material), as shown in Fig. 5 in the main text. A larger capacity indicates that a larger amount of memory or nonlinearity is stored in the reservoir state at the current time T_i.

Data availability

No datasets were generated or analyzed during the current study.

Received: 21 November 2024; Accepted: 19 March 2025;
Published online: 12 April 2025

References

1. Baltz, V. et al. Antiferromagnetic spintronics. *Rev. Mod. Phys.* **90**, 015005 (2018).
2. MacDonald, A. H. & Tsoi, M. Antiferromagnetic metal spintronics. *Philos. Trans. R. Soc. A: Math. Phys. Eng. Sci.* **369**, 3098–3114 (2011).
3. Jungwirth, T. et al. The multiple directions of antiferromagnetic spintronics. *Nat. Phys.* **14**, 200–203 (2018).
4. Jungfleisch, M. B., Zhang, W. & Hoffmann, A. Perspectives of antiferromagnetic spintronics. *Phys. Lett. A* **382**, 865–871 (2018).
5. Fukami, S., Lorenz, V. O. & Gomonay, O. Antiferromagnetic spintronics. *J. Appl. Phys.* **128**, 070401 (2020).
6. Parkin, S. S., Hayashi, M. & Thomas, L. Magnetic domain-wall racetrack memory. *Science* **320**, 190–194 (2008).
7. Allwood, D. A. et al. Magnetic domain-wall logic. *Science* **309**, 1688–1692 (2005).
8. Schryer, N. L. & Walker, L. R. The motion of 180 domain walls in uniform dc magnetic fields. *J. Appl. Phys.* **45**, 5406–5421 (1974).
9. Mougin, A., Cormier, M., Adam, J., Metaxas, P. & Ferré, J. Domain wall mobility, stability and walker breakdown in magnetic nanowires. *Europhys. Lett.* **78**, 57007 (2007).
10. Shiino, T. et al. Antiferromagnetic domain wall motion driven by spin–orbit torques. *Phys. Rev. Lett.* **117**, 087203 (2016).
11. Gomonay, O., Jungwirth, T. & Sinova, J. High antiferromagnetic domain wall velocity induced by néel spin–orbit torques. *Phys. Rev. Lett.* **117**, 017202 (2016).
12. Otxoa, R. M., Atxitia, U., Roy, P. E. & Chubykalo-Fesenko, O. Giant localised spin-peltier effect due to ultrafast domain wall motion in antiferromagnetic metals. *Commun. Phys.* **3**, 31 (2020).
13. Kim, S. K., Tserkovnyak, Y. & Tchernyshyov, O. Propulsion of a domain wall in an antiferromagnet by magnons. *Phys. Rev. B* **90**, 104406 (2014).
14. Rama-Eiroa, R., Otxoa, R. M., Roy, P. E. & Guslienko, K. Y. Steady one-dimensional domain wall motion in biaxial ferromagnets: mapping of the Landau–Lifshitz equation to the sine-Gordon equation. *Phys. Rev. B* **101**, 094416 (2020).
15. Otxoa, R. et al. Walker-like domain wall breakdown in layered antiferromagnets driven by staggered spin–orbit fields. *Commun. Phys.* **3**, 190 (2020).
16. Lee, M.-K., Otxoa, R. M. & Mochizuki, M. Predicted multiple walker breakdowns for current-driven domain-wall motion in antiferromagnets. *Phys. Rev. B* **110**, L020408 (2024).
17. Cheng, R., Daniels, M. W., Zhu, J.-G. & Xiao, D. Ultrafast switching of antiferromagnets via spin-transfer torque. *Phys. Rev. B* **91**, 064423 (2015).
18. Tatara, G., Akosa, C. A. & Otxoa de Zuazola, R. M. Magnon pair emission from a relativistic domain wall in antiferromagnets. *Phys. Rev. Res.* **2**, 043226 (2020).
19. Schwinger, J. On gauge invariance and vacuum polarization. *Phys. Rev.* **82**, 664 (1951).
20. Allor, D., Cohen, T. D. & McGady, D. A. Schwinger mechanism and graphene. *Phys. Rev. D—Part. Fields Gravit. Cosmol.* **78**, 096009 (2008).
21. Schmitt, A. et al. Mesoscopic Klein–Schwinger effect in graphene. *Nat. Phys.* **19**, 830–835 (2023).
22. Roy, P. E., Otxoa, R. M. & Wunderlich, J. Robust picosecond writing of a layered antiferromagnet by staggered spin–orbit fields. *Phys. Rev. B* **94**, 014439 (2016).
23. Gavriloaea, P.-I. et al. Efficient motion of 90° domain walls in Mn_2Au via pure optical torques. arXiv preprint arXiv:2405.09253 (2024).
24. Ross, J. et al. Ultrafast antiferromagnetic switching of Mn_2Au with laser-induced optical torques. *npj Comput. Mater.* **10**, 234 (2024).
25. Ritzmann, U., Desplat, L., Dupé, B., Camley, R. E. & Kim, J.-V. Asymmetric skyrmion-antiskyrmion production in ultrathin ferromagnetic films. *Phys. Rev. B* **102**, 174409 (2020).
26. Otxoa, R. M. et al. Topologically-mediated energy release by relativistic antiferromagnetic solitons. *Phys. Rev. Res.* **3**, 043069 (2021).
27. Otxoa, R. M., Tatara, G., Roy, P. E. & Chubykalo-Fesenko, O. Tailoring elastic and inelastic collisions of relativistic antiferromagnetic domain walls. *Sci. Rep.* **13**, 21153 (2023).
28. Wadley, P. et al. Electrical switching of an antiferromagnet. *Science* **351**, 587–590 (2016).
29. Železny`, J. et al. Relativistic Néel-order fields induced by electrical current in antiferromagnets. *Phys. Rev. Lett.* **113**, 157201 (2014).
30. Torrejon, J. et al. Neuromorphic computing with nanoscale spintronic oscillators. *Nature* **547**, 428–431 (2017).
31. Kanao, T. et al. Reservoir computing on spin-torque oscillator array. *Phys. Rev. Appl.* **12**, 024052 (2019).
32. Marković, D. et al. Reservoir computing with spin-torque nano-oscillators. *Appl. Phys. Lett.* **114**, 012409 (2019).

33. Tsunegi, S. et al. Physical reservoir computing with spin torque and electric double-layer transistor technologies. *Appl. Phys. Lett.* **114**, 164101 (2019).
34. Furuta, T. et al. Macromagnetic simulations of spin-torque oscillator and applications for artificial neural networks. *Phys. Rev. Appl.* **10**, 034063 (2018).
35. Nakane, R., Tanaka, G. & Hirose, A. Reservoir computing with spin waves excited in a garnet film. *IEEE Access* **6**, 4462–4469 (2018).
36. Yamaguchi, T. et al. Reservoir computing with an energy-efficient dynamic memristor for temporal information processing. *Sci. Rep.* **10**, 1–9 (2020).
37. Bourianoff, G., Pinna, D., Sitte, M. & Everschor-Sitte, K. Potential implementation of reservoir computing models based on magnetic skyrmions. *AIP Adv.* **8**, 055602 (2018).
38. Prychynenko, D. et al. Magnetic skyrmion as a nonlinear resistive element: a potential building block for reservoir computing. *Phys. Rev. Appl.* **9**, 014034 (2018).
39. Pinna, D., Bourianoff, G. & Everschor-Sitte, K. Reservoir computing with random skyrmion textures. *Phys. Rev. Appl.* **14**, 054020 (2020).
40. Jiang, W. et al. Reservoir computing with skyrmion memristors. *Appl. Phys. Lett.* **115**, 192403 (2019).
41. Lee, M. K. & Mochizuki, M. Reservoir computing using a skyrmion memristor network. *Phys. Rev. Appl.* **18**, 014074 (2022).
42. Lee, M.-K. & Mochizuki, M. Handwritten digit recognition by spin waves in a skyrmion reservoir. *Sci. Rep.* **13**, 19423 (2023).
43. Yokouchi, T. et al. Skyrmion-based neuromorphic computing. *Sci. Adv.* **8**, eabq5652 (2022).
44. Msiska, R., Love, J., Mulkers, J., Leliaert, J. & Everschor-Sitte, K. Reservoir computing with skyrmions. *Adv. Intell. Syst.* **5**, 2200388 (2023).
45. Tanaka, G. et al. Recent advances in physical reservoir computing: a review. *Neural Netw.* **115**, 100–123 (2019).
46. Nakajima, K. Physical reservoir computing—an introductory perspective. *Jpn. J. Appl. Phys.* **59**, 060501 (2020).
47. Nakajima, K. & Fischer, I. Reservoir computing with spin waves excited in a garnet film. *IEICE Tech. Rep.* **118**, 149–154 (2018).
48. Godinho, J. et al. Antiferromagnetic domain wall memory with neuromorphic functionality. *npj Spintron*. **2** https://www.nature.com/articles/s44306-024-00027-2 (2024).
49. Braun, H.-B. Topological effects in nanomagnetism: from superparamagnetism to chiral quantum solitons. *Adv. Phys.* **61**, 1–116 (2012).
50. López-Ruiz, R., Mancini, H. L. & Calbet, X. A statistical measure of complexity. *Phys. Lett. A* **209**, 321–326 (1995).
51. Dambre, J., Verstraeten, D., Schrauwen, B. & Massar, S. Information processing capacity of dynamical systems. *Sci. Rep.* **2**, 514 (2012).
52. Inubushi, M. & Yoshimura, K. Memory and nonlinearity in dynamical systems with feedback. *Sci. Rep.* **7**, 10199 (2017).
53. Fujii, K. & Nakajima, K. Harnessing disordered-ensemble quantum dynamics for machine learning. *Phys. Rev. Appl.* **8**, 024030 (2017).
54. Strang, G. *Introduction to Linear Algebra*. (Wellesley-Cambridge Press, Wellesley, MA, 1993).

Acknowledgements

J.R. and P.G. acknowledge funding from the European Union's Horizon 2020 research and innovation program under the Marie Skłodowska-Curie International Training Network COMRAD (grant agreement No. 861300). M.M. and M.-K.L. thank the support from Japan Society for the Promotion of Science KAKENHI (Grant Nos. 20H00337, 22H05114 and 24H02231), CREST, the Japan Science and Technology Agency (Grant No. JPMJCR20T1), and a Waseda University Grant for Special Research Projects (Project No. 2024C-153). This paper is a part of the outcomes of research funded by Waseda University Grants for Specific Research Projects (Research proposal No: 2025C-134). U.A. gratefully acknowledges support by grant PID2021-122980OB-C55 and the grant RYC-2020-030605-I funded by MCIN/AEI/10.13039/501100011033 and by "ERDF A way of making Europe" and "ESF Investing in your future".

Author contributions

R.M.O. conceived the idea and designed the study. J.A.V. and R.M.O. carried out the atomistic spin dynamics simulations. M.-K.L. and M.M. facilitated the understanding and implementation of the reservoir computing model. G.T., P.-I.G., J.R., R.F.L.E., and R.W.C. provided valuable comments and interpretations of the atomistic spin dynamics results. J.A.V., D.L., and R.M.O. developed the theoretical framework for the characterization of the chaotic dynamics. J.A.V., M.-K.L., and R.M.O. wrote the initial draft and prepared the figures. All authors reviewed the manuscript and provided comments and/or edited the final version of the draft.

Competing interests

The authors declare no competing interests.

Additional information

Supplementary information The online version contains supplementary material available at https://doi.org/10.1038/s44306-025-00079-y.

Correspondence and requests for materials should be addressed to J. A. Vélez or R. M. Otxoa.